An Assessment of the Surface Longwave Direct Radiative Effect of Airborne Saharan Dust during the NAMMA Field Campaign

R. A. HANSELL,*,+ S. C. TSAY,+ Q. JI,*,+ N. C. HSU,+ M. J. JEONG,+,# S. H. WANG,*,+,@ J. S. REID,& K. N. LIOU,** AND S. C. OU**

* *University of Maryland, College Park, College Park, Maryland*
+ *NASA Goddard Space Flight Center, Greenbelt, Maryland*
# *Goddard Earth Sciences and Technology Center, University of Maryland, Baltimore County, Baltimore, Maryland*
@ *Department of Atmospheric Sciences, National Central University, Chung-Li, Taiwan*
& *Naval Research Laboratory, Monterey, California*
** *Department of Atmospheric and Oceanic Sciences, and Joint Institute for Regional Earth System Science and Engineering, University of California, Los Angeles, Los Angeles, California*

(Manuscript received 16 July 2009, in final form 21 September 2009)

ABSTRACT

In September 2006, NASA Goddard's mobile ground-based laboratories were deployed to Sal Island in Cape Verde (16.73°N, 22.93°W) to support the NASA African Monsoon Multidisciplinary Analysis (NAMMA) field study. The Atmospheric Emitted Radiance Interferometer (AERI), a key instrument for spectrally characterizing the thermal IR, was used to retrieve the dust IR aerosol optical depths (AOTs) in order to examine the diurnal variability of airborne dust with emphasis on three separate dust events. AERI retrievals of dust AOT are compared with those from the coincident/collocated multifilter rotating shadowband radiometer (MFRSR), micropulse lidar (MPL), and NASA Cloud–Aerosol Lidar and Infrared Pathfinder Satellite Observation (CALIPSO) sensors. The retrieved AOTs are then inputted into the Fu–Liou 1D radiative transfer model to evaluate local instantaneous direct longwave radiative effects (DRE_{LW}) of dust at the surface in cloud-free atmospheres and its sensitivity to dust microphysical parameters. The top-of-atmosphere DRE_{LW} and longwave heating rate profiles are also evaluated. Instantaneous surface DRE_{LW} ranges from 2 to 10 W m^{-2} and exhibits a strong linear dependence with dust AOT yielding a DRE_{LW} of 16 W m^{-2} per unit dust AOT. The DRE_{LW} is estimated to be ~42% of the diurnally averaged direct shortwave radiative effect at the surface but of opposite sign, partly compensating for the shortwave losses. Certainly nonnegligible, the authors conclude that DRE_{LW} can significantly impact the atmospheric energetics, representing an important component in the study of regional climate variation.

1. Introduction

For over a decade, there have been many observational and theoretical efforts to determine the radiative impact of airborne mineral dust on the earth–atmosphere system (e.g., Mahowald et al. 2006; Haywood et al. 2003, 2005; Zhang and Christopher 2003; Hsu et al. 2000; Sokolik and Toon 1996a,b; Ackerman and Chung 1992). Less attention, however, has been given to the longwave (LW) contributions, mainly because the shortwave (SW) measurements are easier to make in the field. In addition, the limited experimental data on dust optical properties at infrared wavelengths and the large uncertainties in the spatially and temporally dependent particle properties—size, shape, and composition (Sokolik and Toon 1999)—have indeed made it a difficult challenge to constrain the LW impact.

The term "aerosol radiative forcing" is now commonly used for gauging changes in the radiative fluxes due to anthropogenic aerosols since the beginning of the industrial era (~1750) (Forster et al. 2007). We therefore use the term "direct radiative effect" (DRE) to quantify the difference between radiative fluxes in dust and dust-free atmospheres. In doing so we also maintain consistency with other published literature (e.g., Yu et al. 2006; Haywood et al. 2005).

The overall cooling SW DRE of dust (hereafter DRE_{SW}) has already been studied by a number of

Corresponding author address: Richard A. Hansell Jr., NASA Goddard Space Flight Center, Greenbelt, MD 20771.
E-mail: richard.a.hansell@nasa.gov

DOI: 10.1175/2009JAS3257.1

investigators (e.g., Liu et al. 2003; Tanré et al. 2003; Haywood et al. 2001, 2003; Mohalfi et al. 1998). For conservative scatterers (i.e., no absorption) these effects critically depend on the solar zenith angle (SZA); hence, instantaneous measurements of the SW effect have been commonly converted into a diurnal average (Anderson et al. 2005). For example, based on an analysis of in situ studies, Anderson et al. 2005 estimated the diurnally averaged top-of-atmosphere (TOA) DRE_{SW} for Saharan dust over ocean to lie in the range of -24 to -36 W m^{-2} per unit aerosol optical thickness (AOT), that is, W m^{-2} τ^{-1}. The corresponding surface effect, which is about 1.6 times greater than that at the TOA (Haywood et al. 2003), lies in the approximate range of -38.4 to -57.6 W m^{-2} τ^{-1}.

More recently however, the LW DRE of dust (hereafter DRE_{LW}) has been garnering more attention within the scientific community. Slingo et al. (2006), for example, reported major perturbations in the LW fluxes of a large Saharan dust storm with midday decreases in the outgoing LW radiation (OLR) of ~30 W m^{-2}. Downward thermal emissions from dust were also observed to increase owing to the larger dust particle sizes (Slingo et al. 2006).

Haywood et al. (2005) compared the OLR from the Met Office unified operational numerical weather prediction (NWP) model with that determined from the Earth Radiation Budget Experiment instrument onboard *Meteosat-7*. By including observation-based optical properties of mineral dust in the radiative transfer calculations, Haywood et al. suggested that dust DRE_{LW} can be as large as 50 W m^{-2} in the July monthly mean for 1200 UTC in cloud-free regions over warm desert surfaces.

Lastly, Vogelmann et al. (2003) demonstrated that the daytime surface instantaneous DRE_{LW} observed during the 2001 Aerosol Characterization Experiment in Asia (ACE-ASIA), where dust was a major component of the total aerosol burden, could range from several up to 10 W m^{-2}.

The results of these studies all highlight the significance of the LW contributions of dust, with each having important implications for their potential to modulate the heat and moisture surface budgets (Solomon et al. 2007), surface–air exchange processes, and the general circulation of the atmosphere (e.g., Lau et al. 2006). It is necessary to understand these regional effects before a comprehensive understanding of its global-scale impact can be achieved.

In this paper, the DRE_{LW} of airborne mineral dust during the NASA African Monsoon Multidisciplinary Analysis (NAMMA) 2006 field campaign is investigated to illustrate the significance of the regional LW effects along the west coast of Africa. NAMMA was a part of the overlying AMMA campaign, which was a major international project designed to improve our understanding of the monsoon and the meteorology and climatology of West Africa and its corresponding impacts on health, water resources, and food security in the region (Redelsperger et al. 2006). A comprehensive overview of the dust results during AMMA was recently reported by Haywood et al. 2008.

We mainly focus on the surface DRE_{LW} using combined data from radiative transfer modeling and a comprehensive network of ground-based sensors from NASA Goddard's two mobile ground-based laboratories: Chemical, Optical, and Microphysical Measurements of In Situ Troposphere (COMMIT) and Surface-Sensing Measurements for Atmospheric Radiative Transfer (SMART), which were both deployed on Sal Island in Cape Verde (16.73°N, 22.93°W), located about 560 km off the coast of Senegal in West Africa. We also evaluate the TOA DRE_{LW} and LW heating rate profiles to address the radiative impact over the atmospheric column. It is emphasized that the derived DRE_{LW} of dust presented in this paper are given as instantaneous values for cloud-free atmospheres.

This study examines daytime/nighttime Atmospheric Emitted Radiance Interferometer (AERI) data in the thermal IR window (800–1200 cm^{-1}) for three dust periods, employing the dust detection and IR AOT retrieval methodology presented in Hansell et al. (2008). Appropriate for this region, a dust microphysical model representative of transported Saharan desert dust is adopted, using the refractive index model of Volz (1973). It is recognized, however, that the refractive index of mineral dust may vary considerably (Sokolik and Toon 1999). Highwood et al. (2003), for example, investigated the sensitivity of the LW effect of mineral dust to different refractive index models—including Volz (1973), Fouquart et al. (1987), and World Climate Program (1986)—and found considerable differences in the calculated radiances. Additionally, new methodologies have been developed for determining a mineral dust composite refractive index by mixing kaolinite, quartz, and gypsum and comparing the measured terrestrial spectra from another AERI instrument with spectra computed by a radiative transfer model (Turner 2008). We use the refractive indices of Volz (1973) as a default, but investigate the sensitivity to this assumption along with sensitivity to dust microphysical parameters later. Dust particle sizes were characterized by measurements from the COMMIT ground-based aerodynamical particle sizer (APS 3321); for simplicity, particle shapes were assumed to be spherical.

The instantaneous surface DRE_{LW} of dust is calculated using the NASA Langley modified Fu–Liou radiative transfer code (FL0403 15 April 2003) (Rose and

TABLE 1. Primary instruments.

Instrument	Channels (μm)		Resolution	Reference
	Spectral	Size		
AERI (Bomem)	(1) 3.3–5.5[a] (2) 5.5–18.2	—	1 cm^{-1} spectral;[b] 10 min temporal; 150–250 m vertical	Feltz et al. (2003); Knuteson et al. (2004)
MFRSR (YES)	0.415, 0.5, 0.615, 0.67, 0.87, 0.94, 0.3–1.1[c]	—	1 min temporal[d] hemispherical (2π sr)	Harrison and Michalsky (1994); Alexandrov et al. (2007)[e], McFarlane et al. (2009)[e]
MPLNET (MPL)[f] (GSFC-NASA)	0.532	—	30–60 s temporal 30–75 m vertical	Welton et al. (2001) Campbell et al. (2002)
APS-3321 (TSI)	0.655 laser diode source	0.5–20	0.02 μm at 1 μm 0.03 μm at 10 μm	Reid et al. (2008)
PIR (EPPLEY)	3.5–50	—	1 min temporal Hemispherical (2π sr)	Ji and Tsay (2000)
CALIPSO–CALIOP (NASA CNES)	0.532, 1.064	—	30 m vertical 330 m horizontal Every 16 days	Winker et al. (2007)

[a] AERI has two channels covering the given spectral ranges.
[b] After apodization. Measurement protocol: blackbody scan + scene scan + blackbody scan; 150-m vertical resolution in the lowest 1 km, degrading to 250 m at 3 km (Feltz et al. 2003).
[c] Six narrowband channels (FWHM – 0.010 μm) + 1 broadband channel.
[d] Sampling frequency is 1 Hz with 1-min averaging.
[e] Accuracy ranges from ~ AOT = 0.01 for low aerosol conditions to ~ AOT = 0.20 for heavy aerosol conditions.
[f] See http://mplnet.gsfc.nasa.gov/

Charlock 2002; Fu and Liou 1992, 1993; Su et al. 2008), along with LW heating rates and TOA DRE_{LW}, with measurements at SMART–COMMIT used to constrain the dynamic behavior of the model's atmospheric state.

The organization of this paper is as follows. An overview of the instruments, data, and radiative transfer model is presented in section 2. The dust and meteorological conditions for the three dust periods are briefly examined in section 3. The methodologies used for dust detection/retrieval and for assessing the surface DRE_{LW} are given in section 4. Section 5 presents the results for the dust detection/retrieval, dust surface DRE_{LW}, LW heating rates, TOA DRE_{LW}, and the sensitivity studies to dust microphysics/composition. Finally, a summary is given in section 6.

2. Data (observations and model)

a. Instruments and measurements

Key instruments used in the study include the SMART–COMMIT AERI, a multifilter rotating shadowband radiometer (MFRSR), micropulse lidar (MPL), APS-3321, and precision infrared radiometer (PIR). Details of each instrument can be found online (see http://smart-commit.gsfc.nasa.gov/).

We also use the Cloud–Aerosol Lidar with Orthogonal Polarization (CALIOP), the primary instrument carried by the Cloud–Aerosol Lidar and Infrared Pathfinder Satellite Observation (*CALIPSO*) platform (Winker et al. 2007). CALIOP, a two-wavelength polarization lidar (532 and 1064 nm), provides high-resolution (30–60 m in the troposphere) vertical profiles of backscattering properties of clouds and aerosols, in addition to derived microphysical and optical properties (Vaughan et al. 2004).

Table 1 lists the instruments and their specifications and data from each instrument is shown in Table 2, including their calibrated/processed level-1 and -2 data, respectively.

The MFRSR retrieved AOTs (0.50 μm), which have an estimated accuracy of ~0.01 (Hansell et al. 2003) for low aerosol loading conditions, are computed using the Harrison and Michalsky (1994) technique followed by a cloud removal procedure similar to Smirnov et al. (2000). It is noted, however, that the MFRSR retrieval errors can exceed 0.01 for heavy aerosol loading conditions (Alexandrov et al. 2007; McFarlane et al. 2009). McFarlane et al. (2009) found the MFRSR AOT for dust aerosol in Niamey, Niger, to be underestimated by ~10%–15%, owing to the shadowing of forward scattered radiation; however, we have to rely on the MFRSR measurements, since the AERONET (Holben et al. 1998) sun photometer at Cape Verde was inoperable during NAMMA.

Gridded MPL level-1.5a AOT (0.532 μm) data from MPLNET (available for the entire day) are generated using an interpolation of MPL calibration values constrained by AERONET measurements, although they are less accurate than the daytime products (within 20%; see http://

TABLE 2. Data.

Instrument	Data		Accuracy	Comments
	Acquired (level 1)	Processed (level 2)		
AERI	Radiance[a]	AOT, particle size, composition[b]	~1%	1% of ambient radiance
MFRSR	Irradiance[c]	AOT, particle size, SSA, g	~1%–20%	Errors exceed 1% in heavy dust conditions;
MPL	NRB[d]	AOT	≤20%	
APS-3321	Particle counts	Size, area, volume (mass) distributions	~10%–30%	Particle under sizing
PIR (↓)	Irradiance[c]	Total hemispherical flux	≤4%	Includes dome effect
CALIPSO–CALIOP	NRB[d]	AOT	~40%	Based on assumed 30% uncertainty in aerosol extinction-to-backscatter lidar ratio

[a] Radiance units–brightness temperature (K).
[b] Retrieved parameters include AOT (Hansell et al. 2008; Turner 2008) and size/composition (Turner 2008).
[c] Irradiance units (W m^{-2}).
[d] Normalized relative backscatter.

www.mplnet.gsfc.nasa.gov). Uncertainty in *CALIPSO* AOT measurements is ~40%, based on an assumed 30% uncertainty in the aerosol extinction-to-backscatter lidar ratio (see http://www-calipso.larc.nasa.gov).

b. Radiative transfer model

We use the Langley modified Fu–Liou radiative transfer code (FL0403 15 April 2003) (Rose and Charlock 2002; Fu and Liou 1992, 1993; Su et al. 2008) to calculate the LW surface fluxes for dust and pristine conditions. The model is run using the two-stream/four-stream scheme across 15 SW spectral bands from 0.175 to 4.0 μm and 12 LW bands between 2850 and 0 cm^{-1}. The correlated *k*-distribution method is used to account for nongray gaseous absorption due to H_2O, CO_2, O_3, N_2O, and CH_4 (Fu and Liou 1992). The code also employs a parameterized version of the LW water vapor continuum model (CKD2.4) to account for strong water vapor absorption. Modifications to the code enable time series of retrieved AERI IR AOT (scaled to $\lambda = 0.55$ μm) and combined AERIPLUS [a physical retrieval algorithm developed by the University of Wisconsin Space Science and Engineering Center (UW-SSEC), see Feltz et al. 2003), used to retrieve temperature/moisture profiles from AERI radiances] and radiosonde profiles of pressure, temperature, and water vapor density to be input for calculating the diurnal variability of the dust DRE_{LW}.

Considering the size of Sal Island (~216 km^2) and assuming that it is effectively an ocean site, we use a constant surface albedo/emissivity of 0.02/0.99, respectively, to constrain the model surface boundary conditions. We also input an averaged retrieved ocean surface skin temperature of 26°C for the study period using the NOAA Advanced Very High Resolution Radiometer (AVHRR) Pathfinder (V5) dataset, obtained from the Jet Propulsion Laboratory's physical oceanography Distributed Active Archive Center (DAAC) (see http://poet.jpl.nasa.gov/).

An equivalent spherical (hereafter E-S) dust microphysical model based on the Volz (1973) refractive indices ($\lambda = 2.5$–39 μm) formed the primary aerosol inputs to the code. The spectral range of the refractive indices was extended to cover all band wavelengths in the Fu–Liou model by incorporating the refractive indices from time-averaged AERONET (Holben et al. 1998) retrievals ($\lambda = 0.44$–1.02 μm) at the Cape Verde site over the last 15 years and climatological values ($\lambda = 1.25$–2 μm) from D'Almeida et al. (1991). The dust single-scattering properties were then computed as an average over the Fu–Liou spectral bands (Fig. 1) and the dust vertical distribution was prescribed using an AOT scale height of 3 km.

Dust AOT in the model calculations was based on the AERI-retrieved AOTs scaled from $\lambda = 10$ to $\lambda = 0.55$ μm using an IR-to-visible extinction coefficient ratio [$\beta_{ext}(10\ \mu m)/\beta_{ext}(0.55\ \mu m)$] of ~0.5 using the Volz set of refractive indices for 1.17-μm-sized particles (section 4a). The model dust layers range from the surface up to 3 km

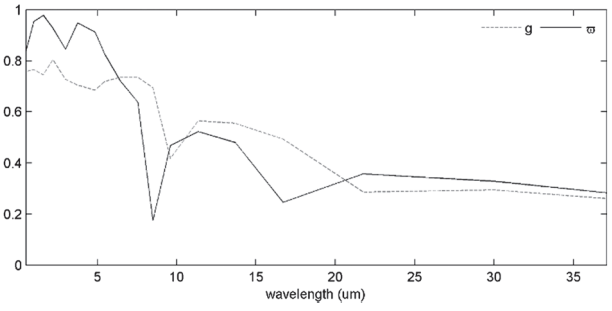

FIG. 1. Dust single-scattering albedo ω and asymmetry factor g as a function of wavelength.

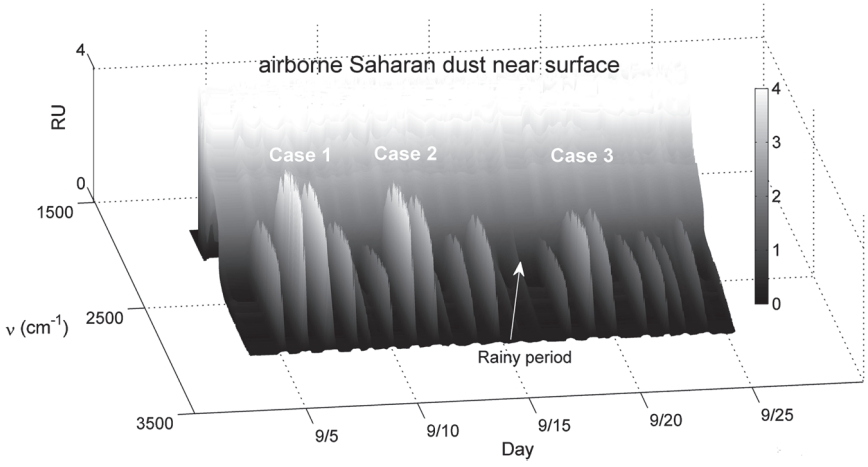

FIG. 2. Dust over Sal Island observed by AERI during NAMMA from enhanced scattering by dust particles from ~1800 to 3000 cm^{-1}. Dust cases 1–3 are shown. Radiance units (RU): mW m^{-2} sr^{-1} (cm^{-1}).

and the dust properties are prescribed to be uniform and homogeneous inside each layer.

Finally, following Hansell et al. (2008), we account for the temporal variability of the thermodynamic state parameters in the column atmosphere (i.e., temperature/relative humidity) by combining AERIPLUS (Feltz et al. 2003) profiles for the first 4 km in the model atmosphere, with regional sounding data using radiosondes launched near SMART–COMMIT, up to a height of ~18 km. For levels above 18 km a climatological midlatitude summer profile (McClatchley et al. 1972) was employed. The model atmosphere is defined over a total of 66 layers with a vertical resolution of 0.1 km up to 900 mb, 0.5 km up to 500 mb, and 5 km to the TOA (0.07 mb).

3. Dust and meteorological conditions during NAMMA

Figure 2 illustrates alternating patterns of daily 3-h averaged AERI spectral (1800–3000 cm^{-1}) radiances mainly due to enhanced scattering of surface dust (Feltz et al. 2003). It is noted that these patterns may also be associated with the propagation of African easterly waves (AEWs) (Jones et al. 2003), a point of interest to the study of dust transport. However, a thorough understanding of the link between these synoptic features and the dust-caused alternating temporal patterns will require further analysis. The scattering intensities are shown to be generally higher during the first half of the SMART–COMMIT deployment, particularly during the periods of 6–8 and 11–14 September (cases 1 and 2, respectively) with weaker peaks observed during the remaining half of the observation period, including the episode of 19–20 September (case 3). Earlier analyses of cases 2 and 3 have been performed by Jeong et al. (2008). The current work specifically focuses on these three active dust periods.

MPL profiles of normalized relative backscatter (NRB) for dust cases 1–3, shown in Figs. 3a–e, reveal a near-surface layer, possibly a mixture of local dust with marine aerosols, and an elevated layer (~2–5 km), perhaps due to entrained dust inside the Saharan air layer (SAL). Below 0.5 km, no readings are shown owing to the near-field observation limits of the MPL (Campbell et al. 2002). The profile in Fig. 3f (21 September) is provided as a reference for depicting minimal dust activity. Scattered high-level cirrus clouds were also observed; however, these appeared to be quite thin and should not affect the surface retrievals (Hansell et al. 2008) since most of the IR signal detected at the surface comes from the lower atmosphere (Feltz et al. 2003).

The thermodynamic structure of the SAL (horizontal layers of dry hot air usually between ~600–800 mb; Prospero 1999; and J. S. Reid et al. 2003), is evident in the AERIPLUS (Feltz et al. 2003) retrieved profiles. Figures 4a and 4b show time–height plots of retrieved ambient temperature T_a and relative humidity during the study period, respectively. The SAL characteristic features are most evident during the three dust periods (boxed regions 1–3) when higher temperatures (shown in Fig. 4a) correspond to lower water vapor amounts (shown in Fig. 4b).

Daytime/nighttime radiosondes were launched daily at the National Institute of Meteorology and Geophysics (INMG) at Cape Verde near SMART–COMMIT. The T_a profiles commonly exhibited sharp inversions from 1 to 2 km, while those for RH featured significant reductions in water vapor concentrations from 1 to 4 km.

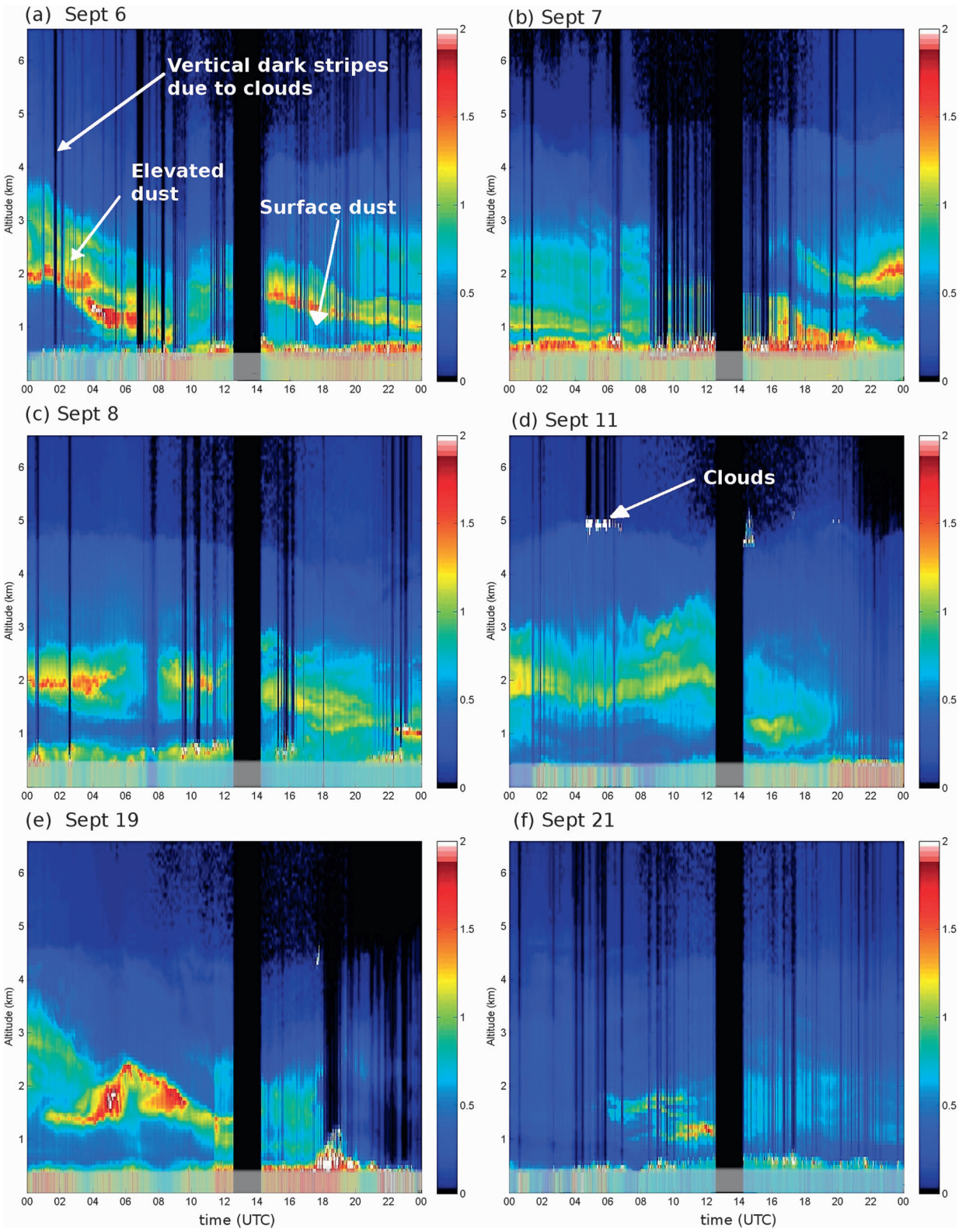

FIG. 3. MPL NRB profiles for (a)–(e) dust cases 1–3 and (f) the minimum dust case; (a)–(e) show the upper and lower dust layers. Dark shaded boxes cover the region below 0.5 km, near-field observation limits of MPL. Dark vertical stripes across images are to due to low clouds near surface. The prominent band (~1200–1400 UTC) is due to a mechanical shade used to protect the MPL optics during solar noon. (Source: MPLNET).

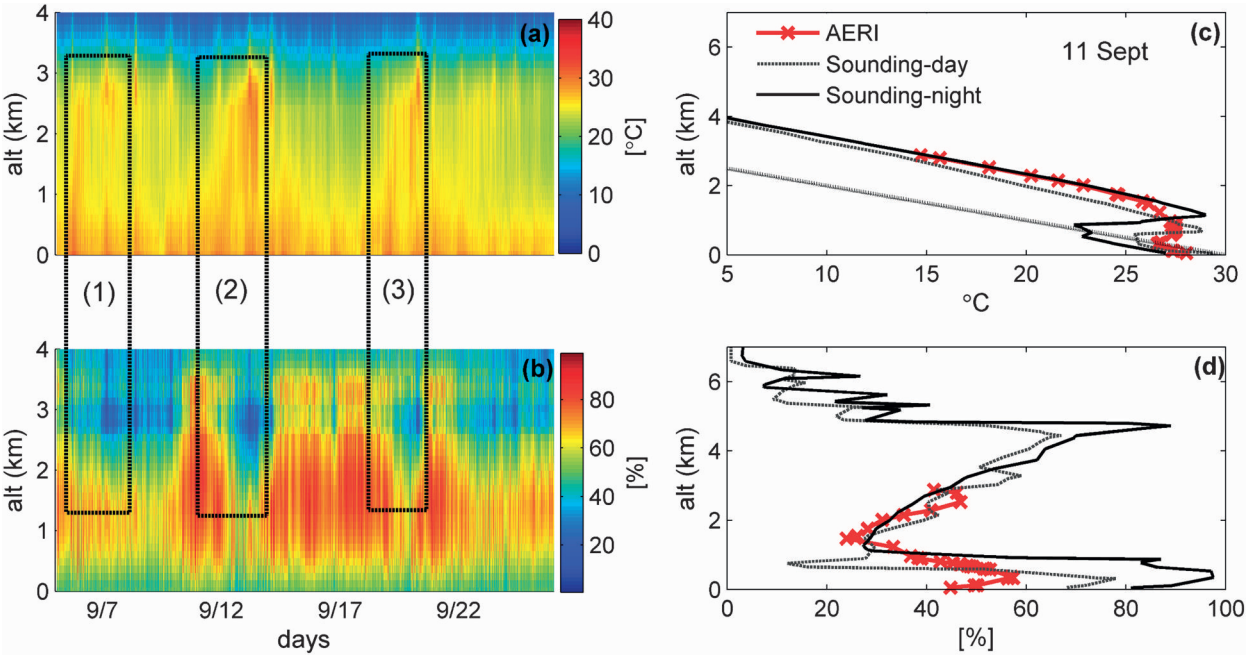

FIG. 4. (a),(b) AERIPLUS-retrieved (a) T_a and (b) RH during NAMMA; the dashed boxes highlight the three dust cases. Example of daytime/nighttime sounding profiles (c) for temperature and (d) for RH on 11 September vs AERI. The dashed line is the dry adiabatic lapse rate (1°C per 100 m). See text for details.

Figures 4c and 4d, for example, show the T_a and RH profiles from daytime/nighttime radiosondes launched on 11 September (case 2). Also plotted are coincident daytime AERIPLUS profiles (red curve) on the same day. Although AERIPLUS retrieved surface RH is ~35% smaller than that from the daytime sounding (gray curve), likely due to using only AERI radiances in the AERIPLUS retrieval, AERI is able to capture the variability in the moisture distribution from ~0.5 to 3 km. On 11 September, the MBL was capped by a strong daytime inversion at 500 m (i.e., air temperature dropped ~3°–4°C within 100 m) on which the dust layers were positioned (Fig. 4c). During the night, the inversion lifted by approximately 300 m. The temperature lapse rate for the dust layers was ~0.62°C per 100 m, indicative of a stable atmosphere.

4. Methodology

a. *Dust detection/retrieval*

Although we do not have direct measurements of sea salt concentrations, derived humidification factors $f(85\%)$ (Jeong et al. 2007, 2008), strongly suggest the presence of hygroscopic particles. Previous studies at Cape Verde reported that, on average, sea salt together with sulfates and carbonaceous aerosols contributed to a background AOT ($\lambda = 0.670\ \mu$m) of only ~0.04 (Chiapello et al. 1999). As a note, the subtropical mean AOT (midvisible wavelengths) for sea salt is ~0.08 (Reid et al. 2006). Although sea salt is a minor component compared to dust, we consider its effects in the dust detection algorithm.

Following a radiance correction scheme (Hansell et al. 2008) to account for the nonlinear effects associated with the AERI channel-1 HgCdTe detector, the BTD 11–10 cloud/dust detection approach, presented in Hansell et al. was applied to over 30 000 AERI spectra to screen for clouds and sea salt.

Figure 5 shows the refractive indices for sea salt (Shettle and Fenn 1979) as a function of relative humidity (RH = 0% and 50%) versus dust (Volz 1973) and water (Warren 1984) across the IR window. The boxed area denotes the spectral region used in the BTD 11–10 approach (Hansell et al. 2008). Note, BTD 11–10 for sea salt at RH = 50% and water are nearly indistinguishable since sea salt is hygroscopic and its refractive index approaches that for pure water in the IR as RH approaches 100%. Since the averaged surface RH measured at SMART–COMMIT was ~74 ± 10% (second half of September), the BTD 11–10 technique can be effectively employed to remove the effects of sea salt from the AERI spectra.

After applying the BTD 11–10 method, ~20% of the AERI spectra were classified as cloud free while the remaining data was discarded owing to either heavy cloud cover and/or extensive sea salt conditions. Following Hansell et al. (2008), the IR AOT time series was retrieved

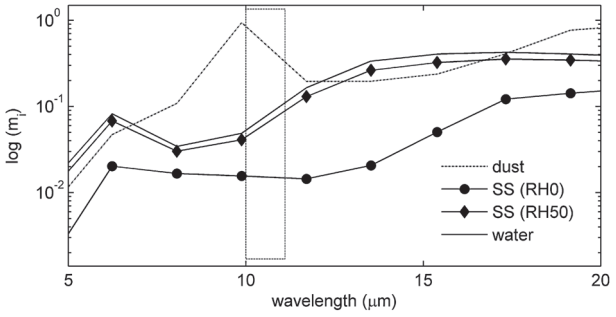

FIG. 5. Comparison of refractive indices (logarithm of imaginary component) for sea salt (SS), dust, and water. Sea salt is shown as a function of relative humidity for RH = 0% and 50%. The dotted box denotes the spectral region used in the BTD 11–10 dust/cloud detection scheme (Hansell et al. 2008).

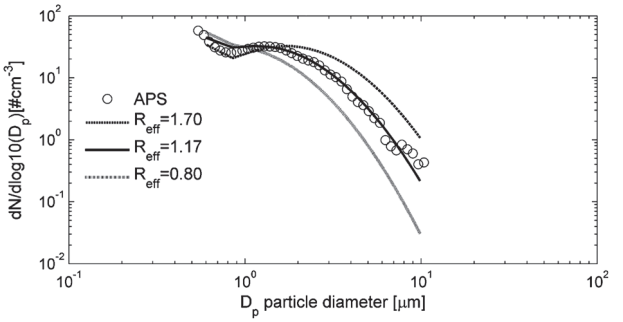

FIG. 6. Best-fit (solid curve) APS size distribution, measured during surface dust event on 19 Sep, and adjusted (broken curves) size distributions used in the sensitivity study. See text for details.

using the cloud-free spectra coinciding with the three dust periods. We retrieve the IR AOT about every hour. For comparison, two additional days (10 and 21 September) with relatively thin dust (τ_{thin}) as measured by the MFRSR at 0.50 μm ($\tau_{\text{thin}} \sim 0.29 \pm 0.04$ compared with $\tau \sim 0.57 \pm 0.07$ for the three dust periods) were evaluated.

Dust particle sizes were characterized by a best fit to the APS data (particle number concentration N cm^{-3}) for dust case 3 (19 September; Fig. 6). Size spectra for the other days exhibited similar distributions. The size distribution shows two particle size modes with fitting parameters: $r_{\text{eff1}} = 1.17$ μm, $\sigma_1 = 1.96$, and $N_1 = 55$ and $r_{\text{eff2}} = 0.25$ μm, $\sigma_2 = 1.44$, and $N_2 = 400$ for coarse and fine modes, respectively, where $r_{\text{eff1/2}}$, $\sigma_{1/2}$ and $N_{1/2}$ are the effective radius, effective geometric standard deviation, and total particle number for the two modes, respectively [note that the volume mean diameter (VMD) for this size distribution is ~2.8 μm]. Here we refer to coarse-mode particles as those having effective diameters of at least 0.8 μm (Reid et al. 2008). The parameters suggest that this case was largely dominated by the fine mode for which larger particles underwent gravitational sedimentation during transport.

We examined the sensitivity of the retrieval to variations in the effective radius for coarse mode particles (r_{eff1}) while holding the fine mode constant, assuming that σ and N do not change significantly (i.e., the shape of the distribution is preserved). The effective size was perturbed ~0.5 μm above and below the best-fit value (1.17 μm) to simulate a range of realistic particle sizes (0.8–1.70 μm) consistent with observations. Figure 6 shows the range of size distributions given by the broken curves. For the case examined, the size variations produced a small change in the retrieved AOT of less than 1%, although the relative error at one time during the retrieval reached as high as 2%. The sensitivity of surface DRE_{LW} to changes in particle size is discussed in section 5.

Although an E-S particle approximation is employed, we investigated the effect of particle asphericity on the retrieval to identify the level of uncertainty in the DRE calculations. Here particle asphericity was measured in terms of a monodisperse shape distribution of oblate spheroids having an aspect ratio of 2.2, which is consistent with results from past field observations for Africa (E. A. Reid et al. 2003). The T-matrix light-scattering code (Mishchenko and Travis 1994) was used to calculate the single-scattering properties of dust particles with sizes corresponding to the APS size bins (0.542–19.81 μm). Subsequently, the bulk (mean) optical properties were obtained after integrating the single-scattering properties over the APS size distribution (Fig. 6), following the methodology in Hansell et al. (2008). For the case examined, a distribution of oblate spheroids yielded AOTs that were approximately 5% greater than those for spheres, assuming all other parameters were held constant. Differences were related to larger particle extinction and single-scattering albedo for oblate spheroids across the window region. The associated impact on surface DRE_{LW} is discussed in section 5.

b. DRE_{LW}

We define the surface DRE_{LW} of mineral dust to be the difference in the downwelling (↓) radiative flux at the surface between a dust-laden atmosphere and a clear (pristine) atmospheric reference free of dust. This is given by the expression

$$\Delta F\downarrow = F_{\text{all-sky}}\downarrow - F_{\text{clear}}\downarrow, \quad (1)$$

where ΔF represents the calculated instantaneous DRE (W m^{-2}), $F_{\text{all-sky}}$ is the flux for all-sky conditions (i.e., $F_{\text{all-sky}} = F_{\text{dust}} + F_{\text{clear}}$), and F_{clear} is the clear-sky flux,

which includes all water vapor (F_{wv}) and trace gas (F_g) contributions. Equation (1) can therefore be rewritten as

$$\Delta F\downarrow = (F_{dust} + F_{wv} + F_g)\downarrow - (F_{wv} + F_g)\downarrow, \qquad (2)$$

where, for the model considerations in this study, it can be shown that ΔF is directly related to F_{dust}. By the sign convention employed, dust will have a positive DRE_{LW} at the surface, which for comparison purposes is consistent with other literature (e.g., Vogelmann et al. 2003).

By convention, DRE is usually defined as the net flux (i.e., down$\downarrow$ − up$\uparrow$) difference between an atmosphere with and without aerosol. Omitting the upward surface fluxes introduces a small difference of ~0.5 W m^{-2}. Because clouds, sea salt, and dust aerosol were always present, observed clear-sky references were not available and had to be calculated using a model atmosphere.

Precipitable water vapor (PWV) is a large source of error when assessing the aerosol radiative effects in the thermal IR window (800–1200 cm^{-1}) due to the strong absorption properties of the water vapor continuum. Large changes in PWV can significantly alter the downwelling radiances, and hence flux, if not properly taken into account. As shown by Eq. (2), the modeled DRE_{LW} is not sensitive to clear-sky atmospheres; however, if one is using observations, (e.g., Hsu et al. 2000; Zhang and Christopher 2003; Hansell et al. 2003) to calculate the surface DRE_{LW}, a moderately large PWV with high temporal variability can significantly bias the results. Several precautions can be met to minimize such impact including 1) restricting the observed dataset to those times when the PWV falls below a prescribed threshold and 2) employing only the observed data where the variability in PWV is minimal or effectively constant.

For heavy loadings of mineral dust, the main source of surface LW flux in the 8–12-μm atmospheric window comes from dust emissions, a direct result of the strong mineral absorption in the thermal IR. It has also been shown in previous work (Dufresne et al. 2002) that the LW scattering effects of dust, particularly for particles in the size range from 0.5 to 10 μm, can exert a significant influence on the surface and TOA DRE_{LW}. Since this size range includes particles found near source regions and in transported dust plumes, the LW scattering effect should be taken into account when modeling dust. Dufresne et al. (2002) show that neglecting LW scattering produces an absolute error of ~5 W m^{-2} at the surface or about a 15% reduction in the received surface flux; hence the surface DRE_{LW} can be underestimated by up to 5 W m^{-2}, a significant amount compared to the total (scattered + absorbed/emitted) surface DRE_{LW}. In the current study, we consider scattering and absorption/emission by the dust layers.

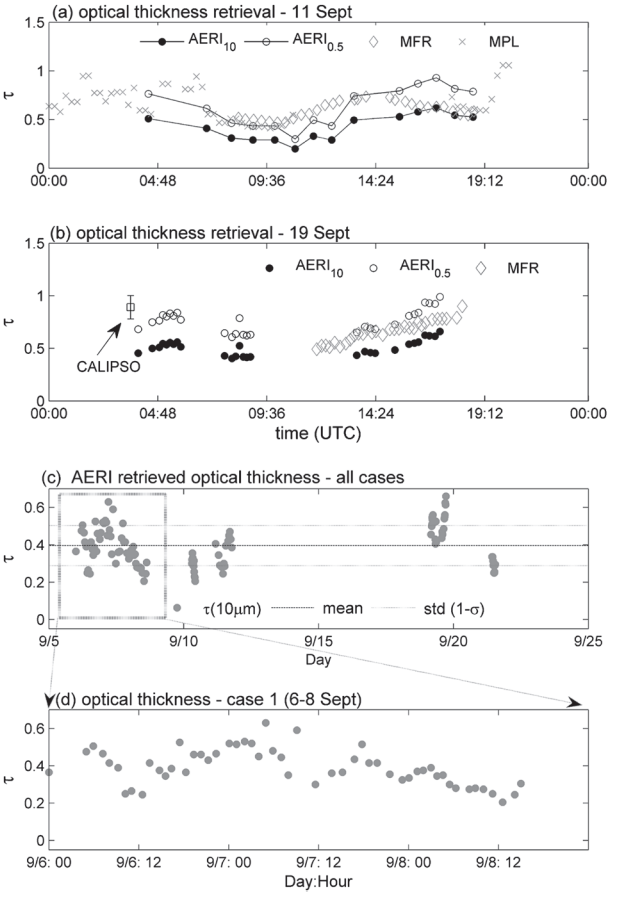

FIG. 7. AERI-retrieved IR AOT (10 μm/0.5 μm-scaled): (a) 11 Sep shown compared with MPL and MFR retrieved AOT at 0.5 μm and (b) 19 Sep shown compared with MFRSR and *CALIPSO* retrieved AOT at 0.5 μm. (c) AERI-retrieved AOT (10 μm) for all cases and (d) magnified view of dust period 1 (6–8 Sep). See text for details.

5. Results

a. Dust detection and retrieval

Examples of daytime/nighttime AERI-retrieved IR AOT compared with collocated ground/satellite-based retrievals are given for two dust cases (11 and 19 September). Figure 7a shows the AERI AOT at 10 and 0.5 μm (scaled) for 11 September, plotted against the combined nighttime/daytime AOT retrievals using collocated MPL level-1.5 and MFRSR data at 0.5 μm, respectively. AERI is able to capture the diurnal variability in the dust loading remarkably well. Deviations of the AERI-scaled AOT with those from the MFRSR, seen mostly during the daytime hours (~1000–1330 UTC), are likely due to increased scattering at shorter wavelengths. AERI-retrieved optical depths are also larger in the late afternoon, indicative of increased surface dust loading (Fig. 3d).

Figure 7b shows the AERI-retrieved AOT at 10 and 0.5 μm (scaled) for 19 September, compared to the visible AOT (0.5 μm) retrieved by the MFRSR. Overall, the dust trends of both instruments show good daytime agreement, particularly between the hours of 1400 and 1800 UTC when each shows a rapid increase in AOT. Similarly, Jeong et al. (2008) reported sharp increases in the scattering coefficients and mass concentrations for dust. The retrieved AOT of AERI and the MFRSR diverge around 1600 UTC, with those from AERI (scaled) being greater than the MFRSR, which could be due to enhanced dust absorption. Jeong et al. also found the dust single-scattering albedo to be decreasing during this time (~0.98 to 0.96), indicative of more absorbing particles. During the nighttime, AERI detects a moderate amount of dust activity ($\tau \sim 0.4$–0.5) around 0400–0500 UTC. For comparison, we use the level-2 AOT measurements (532 nm) from *CALIPSO* (black square) at 0325:44 UTC, nearly coincident with the first AERI retrieval at 0355:59 UTC, to identify surface dust near Sal Island (Note that for the dust periods investigated, only one coincident overpass was identified near the Cape Verde Islands). An averaged AOT ($\tau = 0.891 \pm 0.111$) was computed for 18 subsampled points along the *CALIPSO* track (16°–17°N, 20.5 ± 0.1°W) about 2° east of Sal Island, all within the 10–90 percentile range. Applying the IR/visible extinction coefficient ratio (Hansell et al. 2008), the nearest AERI AOT would scale to ~0.70 at 0.55 μm. One possible reason for the larger *CALIPSO* AOT is the lidar's longer extinctive path length, whereas the thermal emissions that AERI detects are mostly from the lower atmosphere (Feltz et al. 2003).

Time series of AERI-retrieved IR AOT for all cases examined are shown in Fig. 7c, with an average value of ~0.37 ± 0.09. Note the highest AOT was associated with dust case 3 (19 September), reaching as high as ~0.7 (10 μm) or ~1.0 (0.55 μm). Interestingly, dust case 1 (6–8 September) provided three consecutive days of retrieved AOT. A magnified view of this period (Fig. 7d) shows evidence of a diurnal cycle, which appears to exhibit maximum (minimum) values during the nighttime (daytime). These regional dust trends could in part be explained by 1) diurnal changes in the depth of the boundary layer, which could affect the dust loading, and/or 2) an increase in the nighttime dust loading itself. It is possible that dust radiative feedbacks on the Saharan boundary layer dynamics could also be responsible (Heinold et al. 2008).

b. *Surface DRE_{LW} results and sensitivity to dust parameters*

Results of the dust surface DRE_{LW} calculations are presented for the three dust cases. To put these results into context, we also include a short assessment of the associated TOA DRE_{LW} and model-derived LW heating rates. Last, results of the sensitivity of the surface DRE_{LW} to perturbations in dust composition, effective size, and particle asphericity are examined.

1) SURFACE DRE_{LW} RESULTS

We first compare the model surface LW fluxes with those measured from a collocated PIR at SMART–COMMIT to validate the model calculations. Estimated measurement uncertainties of the PIR are ≤3%. The thermal dome effect (Ji and Tsay 2000) and the hourly averaging of the LW fluxes may also contribute a small amount of uncertainty (<1%) in the measurements. Primary model uncertainties include the AERIPLUS-retrieved water vapor/temperature profiles and the dust composition/vertical distribution. For purposes of comparison, we define a best fit when the model fluxes are conservatively within 5% of the measurements, accounting for both PIR and model uncertainties. Although this occurs for a greater number of the fine-mode particles (Fig. 6), it is the larger particles in the coarse mode that directly affect the DRE_{LW}. A best fit is obtained when size parameters r_{eff1} and N_1 are 0.50 μm and 55 cm^{-3}, respectively. (Note that the differences with Fig. 6 are due to instrumental and model uncertainties.) The same effective size was used to calculate the surface DRE_{LW} for the remaining dust cases.

Comparison of the model (with dust) with the PIR LW fluxes and the corresponding scatterplot for case 3 (19 September) are shown respectively in Figs. 8a and 8b, with a correlation coefficient of 0.93. The model was run with and without dust in order to calculate the instantaneous surface DRE_{LW} for 19 September. Figure 8c illustrates the diurnal trend in the surface DRE_{LW}, which is consistent with the AERI-retrieved AOTs shown in Fig. 7b. The maximum and daily mean DRE_{LW} are ~10 and 8 W m^{-2}, respectively. The increases in surface DRE_{LW} in the late afternoon are related to the same increases in dust measurements reported by Jeong et al. (2008) for 19 September. The surface DRE_{LW} for all cases examined is given in Fig. 8d, along with the average and 1-σ standard deviation (~6.8 ± 2 W m^{-2}). The range in surface DRE_{LW} extends from ~2 to 10 W m^{-2}, coinciding with the minimum dust case on 10 September and dust case 1, respectively.

The nighttime surface DRE_{LW}, on average, was found to be larger than that for daytime by about 1.5 W m^{-2}, with daytime/nighttime means of 6.9 and 8.4 W m^{-2}, respectively. This suggests possible changes in the boundary layer thermal structure and the dust loading and altitude, which affect the dust's effective emission temperature. The surface DRE_{LW} for the dust cases is about

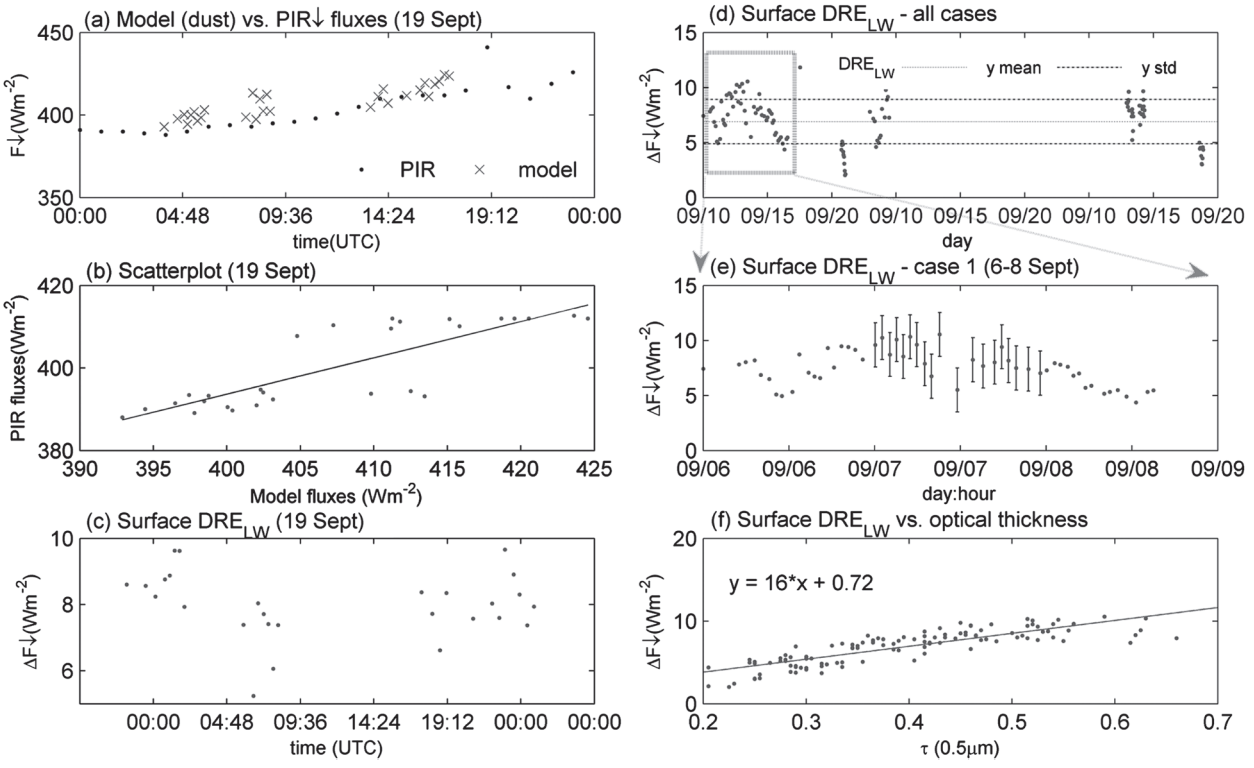

FIG. 8. (a) Model ($r_{\text{eff1}} = 0.5\ \mu$m) vs PIR downward fluxes (19 Sep), (b) scatterplot (19 Sep), (c) surface DRE_{LW} (19 Sep), (d) surface DRE_{LW} for all cases, and (e) surface DRE_{LW} for 6–8 Sep. Error bars depict particle size uncertainty. (f) Surface DRE_{LW} vs retrieved dust AOT (scaled to 0.5 μm). See text for details.

a factor of 2 greater than those for the minimum dust cases (10 and 21 September). The diurnal trends of surface DRE_{LW} for the three consecutive dust days (6–8 September) are shown in Fig. 8e, with error bars given (shown for 7 September for clarity) to depict a particle size uncertainty of nearly ± 2 W m^{-2}, which we address in section 4b.

Surface DRE_{LW} is plotted against dust AOT for the entire study (Fig. 8f), which shows a strong linear dependence with a correlation coefficient of 0.86. In the current study the DRE_{LW} is found to be ~16 W m^{-2} per unit AOT (W m^{-2} τ^{-1}); however, we note that, if the linear regression is forced through zero, the DRE_{LW} increases to 17 W m^{-2} τ^{-1}. For comparison, Haywood et al. (2003) estimated a surface DRE_{SW} of -209 W m^{-2} during the Saharan Dust Experiment (SHADE) field campaign around Cape Verde. Based on the methods of Anderson et al. (2005), the diurnally averaged DRE_{SW} is about -38.4 W m^{-2} τ^{-1}. Considering the meteorological and dust conditions to be comparable during both field studies (both were conducted in September), the derived DRE_{LW} (over ocean) from NAMMA is ~42% of the diurnally averaged DRE_{SW} measured during SHADE.

We point out that the DRE_{LW} changes by ~2 W m^{-2} τ^{-1} when the model's AOT scale height is adjusted from 2 to 4 km and, thus, still represents a significant fraction of the diurnally averaged DRE_{SW}. Although smaller than the DRE_{SW}, the DRE_{LW} can have a measurable impact on the local radiative budget, which can offset the SW cooling. A summary of the dust surface DRE_{LW} found for this study, along with the surface DRE_{LW} obtained from previous works, is presented in Table 3.

2) TOA DRE_{LW} RESULTS

Employing the same model parameters used to calculate surface DRE_{LW}, we determine the DRE_{LW} of the OLR at the TOA and compare our results with previous studies. Consistent with other literature (e.g., Zhang and Christopher 2003; Haywood et al. 2005), the TOA DRE_{LW} is defined as the difference in the upwelling ($\uparrow$) radiative flux at the TOA between a clear (pristine) atmospheric reference free of dust and a dust-laden atmosphere. It is given by

$$\Delta F\uparrow = F_{\text{clear}}\uparrow - F_{\text{all-sky}}\uparrow, \tag{3}$$

where ΔF represents the calculated instantaneous DRE (W m^{-2}).

TABLE 3. Surface DRE_{LW} from previous studies.

Study	DRE_{LW} (W m^{-2})	Surface[a]	Month	Obs platform	Comments
Current[b]	2–10	O	Sep	Ground	Daytime/Nighttime instantaneous DRE – Saharan dust
Vogelmann[c]	Several–10	O	Mar–Apr	Ship	Daytime instantaneous DRE-aerosol in Asia (includes dust)
Highwood[d]	11.5	O/L	Sep	Aircraft	Daytime avg of large Saharan dust event on 25 Sep 2000
Sokolik[e]	3–7 (mild dust) 15–25 (heavy dust)	—	—	—	Modeling study for different regions under variable atmospheric conditions

[a] O-ocean surface; L-land surface.
[b] NAMMA (2006).
[c] Vogelmann et al. (2003): ACE-ASIA (2001).
[d] Highwood et al. (2003): SHADE (2000).
[e] Sokolik and Toon (1997): Modeling study.

Figure 9a shows the instantaneous TOA DRE_{LW} for the three dust cases, with an average plus 1-σ deviation of $+7.0 \pm 2.0$ W m^{-2} and a range of 2–11 W m^{-2}. The TOA DRE_{LW} is plotted against dust AOT for the entire study (Fig. 9b), which (like the surface DRE_{LW}) shows a strong linear dependence with a correlation coefficient of 0.88. The LW flux enhancement at the surface [section 5b(1)] is seen as a reduction in the OLR due to absorption by the dust layers. Per unit AOT, the TOA DRE_{LW} is found to be $\sim$13 W m^{-2} τ^{-1}. When compared to the diurnally averaged DRE_{SW} of Saharan dust (-24 to -36 W m^{-2} τ^{-1}; Haywood et al. 2003) reported by Anderson et al. (2005), the LW perturbation to the radiative budget becomes quite significant (>36%), especially considering that the DRE_{LW} is effective over a full 24-h period. A summary of the dust TOA DRE_{LW} found for this study, along with the TOA DRE_{LW} obtained from previous works, is presented in Table 4. Finally, comparisons of the daily averaged surface and TOA DRE_{LW} for each dust case are given in Table 5, along with the corresponding retrieved IR AOTs at 10 μm.

3) HEATING RATES

Using the Fu–Liou model, we calculate the LW perturbation in the instantaneous heating rates due to the presence of dust by differencing the all-sky (clear sky + dust) and clear-sky heating rates for the model layers. Figure 10 shows the minimum, maximum, and averaged LW heating rate profiles for the three dust cases below 5 km in the lower troposphere. For reference, the minimal dust day (10 September) is shown. Strong peaks in the heating profiles occur in the lowest layers between 0.5 and 0.6 km owing to the large absorption by surface dust. Note the reduced peak on 10 September as a result of the smaller dust AOTs (Fig. 7c). On average, the LW surface heating for the three dust cases varied from 0.25 to 0.30 K day^{-1}, with maximum heating reaching nearly 0.6 K day^{-1} on 6 September (from case 1). These results are similar to those obtained by Highwood et al. (2003) during their study of Saharan dust during SHADE, where they reported a relative warming rate of up to 0.5 K day^{-1} below the dust layers. The average LW heating rate ($\Delta T/\Delta t \cong 0.28$ K day^{-1}) can be translated to a surface DRE_{LW} (ΔF) via the equation

$$\Delta F = -\rho C_p \Delta Z \frac{\Delta T}{\Delta t}, \tag{4}$$

where ρ is the air density, C_p the specific heat capacity of air at constant pressure, and ΔZ the dust layer thickness. Over a 24-h period, the surface DRE_{LW} ranges from 2 to 10 W m^{-2} for dust layers with thickness between 0.5 and 3 km, respectively, roughly the thickness observed by the MPL.

With the exception of 10 September, all average profiles exhibit positive heating from the surface to a height

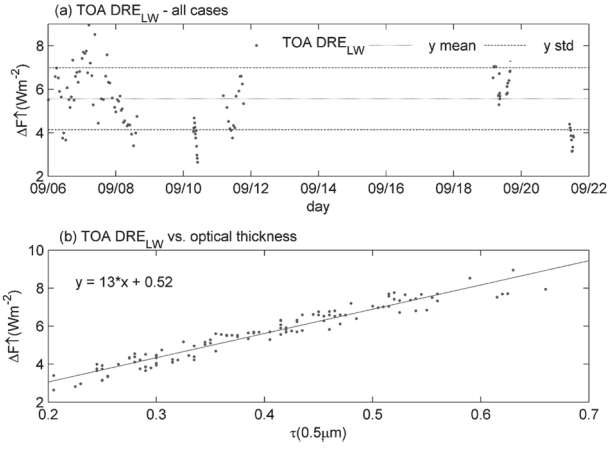

FIG. 9. (a) TOA DRE_{LW} during NAMMA and (b) TOA DRE_{LW} vs retrieved dust AOT (scaled to 0.5 μm): TOA DRE_{LW} defined per Eq. (3). See text for details.

TABLE 4. TOA DRE_{LW} from previous studies.

Study	DRE_{LW} (W m^{-2})	Surface[a]	Month	Obs. platform	Comments
Current[b]	2–11	O	Sep	Ground	Range of instantaneous day/nighttime DRE
	7.4	O	Sep	Ground	Monthly mean
	13	O	Sep	Ground	DRE (W m^{-2} τ^{-1})
Zhang and Christopher[c]	7	L	Sep	Satellite	Monthly mean for six regions over Africa
	15	L	Sep	Satellite	DRE (W m^{-2} τ^{-1}) over Africa
Brindley[d]	17 ± 5	L	May–Jun	Satellite	DRE (W m^{-2} τ^{-1}) over Africa
Hsu[e]	3–12	O	Jul	Satellite	Monthly DRE of Saharan dust
	5–30	O	Jul	Satellite	Daily DRE of Saharan dust

[a] O-ocean surface; L-land surface.
[b] NAMMA (2006).
[c] Zhang and Christopher (2003).
[d] Brindley (2007).
[e] Hsu et al. (2000).

of about 1.5–2.0 km. Elevated dust, which may be entrained in the SAL, could explain the additional heating on 10 September and for those cases whose profiles display positive secondary peaks at higher altitudes. Areas of negative heating are likely associated with radiative cooling of the dust layers. Strong peaks in the heating profiles demonstrate the potential for dust to impact the surface temperatures and stability of the atmosphere through surface–air exchange processes.

4) SENSITIVITY TO DUST PARAMETERS

(i) Particle composition

Five dust models were employed, each having a uniquely defined set of refractive indices corresponding to pure quartz (Q), quartz internally mixed with 10% hematite (Q/H), and the clays illite (I), montmorillonite (M), and kaolinite (K). Although in reality dust particles are usually heterogeneous mixtures of many minerals, the analysis illustrates the large sensitivity of surface DRE_{LW} to dust particles defined by a single composition.

The bimodal lognormal size distribution from 19 September (Fig. 6) was used assuming E-S particles. For each composition, the surface DRE_{LW} was calculated for AOT (τ) 0.05, 0.1, 0.2, 0.4, 0.8, and 1.0. We use the Fu–Liou model's built-in desert-atmospheric profile, a constant surface albedo of 0.2 (from past spectroradiometer reflectance measurements) over the 15-SW bands, and an averaged surface emissivity of 0.98 (using the JPL ASTER spectral library for a quartz surface) over the 10 LW bands. Figure 11a shows the sensitivity of the surface DRE_{LW} to dust particle composition as a function of AOT. Each curve is marked according to mineral type. DRE_{LW} increases as AOT increases with a near-linear relationship. Interestingly, for the minerals evaluated, all except for illite exhibited a larger surface DRE_{LW} than Volz, ranging from ~0.5 W m^{-2} in optically thin dust (τ = 0.05) to ~20 W m^{-2} for heavy dust conditions (τ = 1.0). The large differences in surface DRE_{LW} may be attributed to the unique absorption features associated with pure minerals in the thermal IR (e.g., the classic absorption feature of quartz centered at 9.2 μm), whereas for bulk dust samples (e.g., Volz) the spectrum gets smoothed out owing to internal mixing of the component minerals. Illite is virtually indistinguishable from the Volz mineralogy, which is not surprising since illite was a primary component in the samples analyzed by Volz (1973). The quartz/hematite mixture exhibits the largest DRE_{LW}, followed by the clays kaolinite and montmorillonite. The surface DRE_{LW} for pure quartz also exceeds that for Volz, with relative differences of ~0.5–3.0 W m^{-2} over the range of AOT. Clearly, the associated errors in the surface DRE_{LW} can be quite large depending on the component minerals and how they are partitioned. Employing the Volz refractive indices for this study is probably adequate, particularly since our measurements from Cape Verde are representative of transported Saharan dust, although errors in exact mineral composition are expected and

TABLE 5. Daily averaged surface/TOA DRE_{LW} during NAMMA.

Day	Case	IR AOT (10 μm)	Surface DRE_{LW}[a]	TOA DRE_{LW}[a,b]
6 Sep	1	0.40	+7.5	+9.1
7 Sep	1	0.45	+8.5	+9.1
8 Sep	1	0.31	+6.1	+6.4
10 Sep	Ref[c]	0.27	+3.8	+5.0
11 Sep	2	0.36	+7.0	+8.0
19 Sep	3	0.51	+8.1	+9.6
21 Sep	Ref[c]	0.29	+4.1	+4.8
Mean		0.37	+6.4	+7.4

[a] Units: W m^{-2}.
[b] TOA DRE_{LW} defined per Eq. (3).
[c] Reference: minimum dust case.

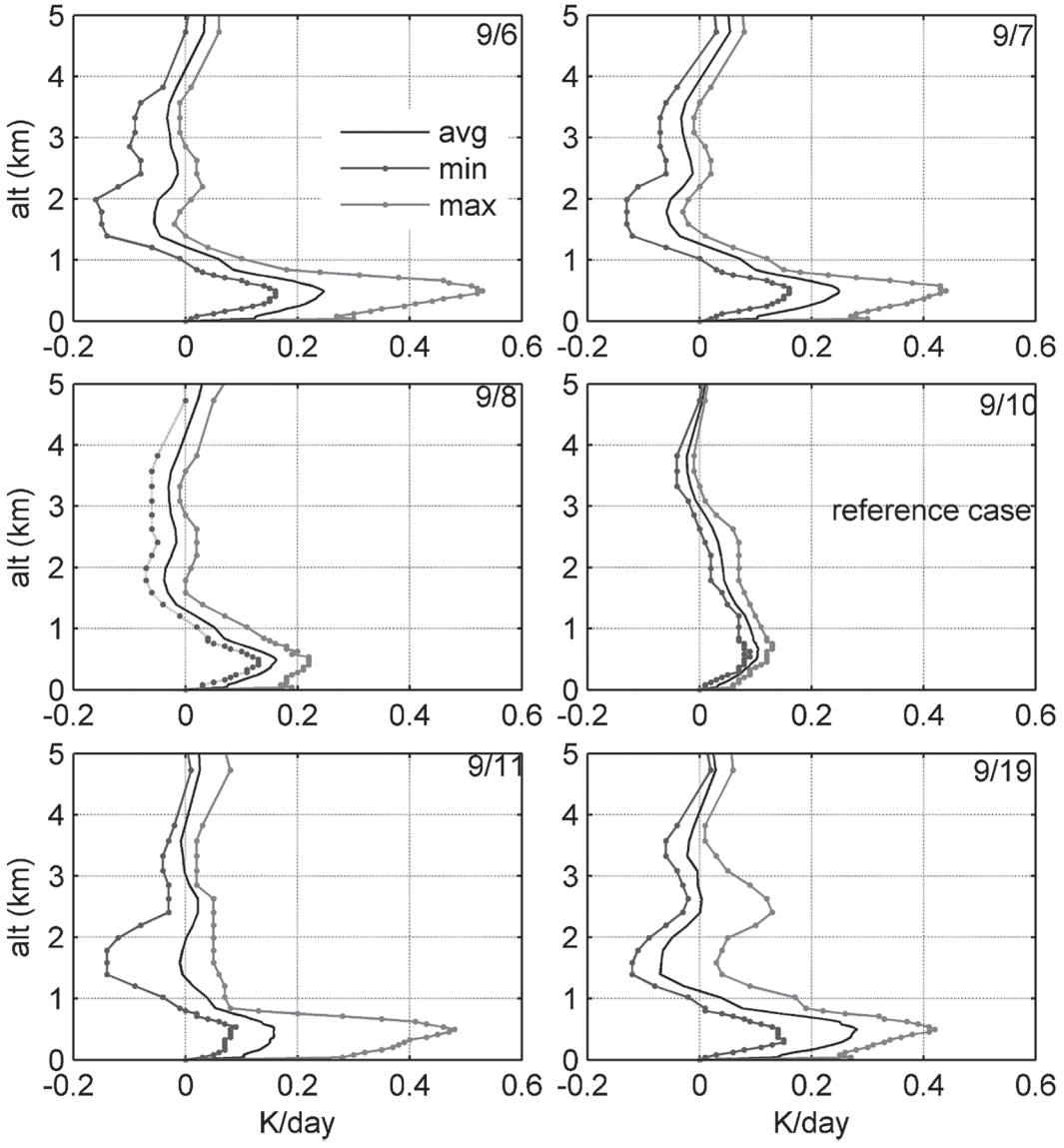

FIG. 10. (a) Calculated LW dust heating rates (all-sky − clear-sky) for each dust case. The minimal dust case (10 Sep) is shown for reference. See text for details.

will depend on which minerals are dominant and how the minerals get mixed.

(ii) Particle size

Three bimodal lognormal size distributions were used to test the sensitivity of surface DRE_{LW} to particle size. Similar to the discussion in section 4, the size parameters (r_{eff1}, σ_{g1}) for coarse-mode particles were iteratively adjusted, covering a range of effective radii—0.80, 1.17, and 1.70 μm with $\sigma_g = 1.96$—while keeping those for the fine-mode ($r_{eff2} = 0.25$ μm, $\sigma_{g2} = 1.44$) constant. Additionally, size distributions with smaller coarse-mode contributions were evaluated using the size parameters $r_{eff1} = 0.25$ and 0.50 μm with $\sigma_{g1} = 1.96$. The Volz refractive indices (Volz 1973) defined the mineral composition, and particles were assumed to be E-S. Figure 11b shows the range of surface DRE_{LW} computed (average ± 1-σ standard deviation) for each size distribution using dust case 3. When particle size increases, so too does the surface DRE_{LW}, where LW scattering and absorption are enhanced. The size distribution in Fig. 6 and the model fit to the PIR data (Fig. 8a) suggest that, although the fine-mode particles ($\leq$0.5 μm) were more dominant during NAMMA, it is the larger particles in the size distribution that impact the DRE_{LW}. For particles in the size range of ~0.25–0.79 μm, Fig. 11b shows that the estimated error

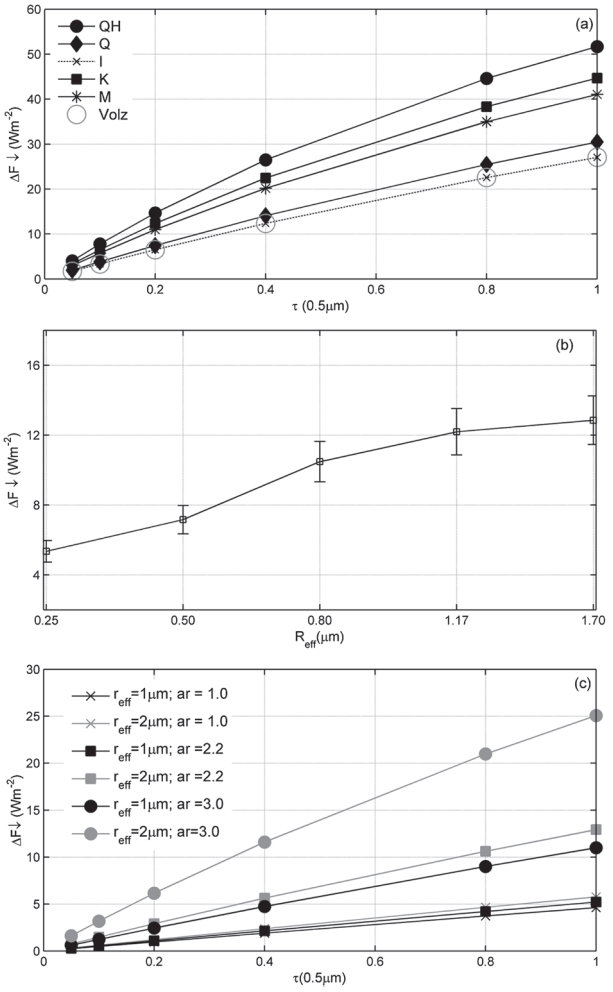

FIG. 11. (a) Sensitivity of surface DRE_{LW} to dust mineralogy. As in (a) but (b) for dust effective size and (c) for particle shape with variable aspect ratios (ar). See text for details.

in surface DRE_{LW} is approximately ± 2 W m^{-2}. The surface DRE_{LW} error increases when coarse-mode particles are dominant and can introduce an additional 5 W m^{-2} of uncertainty for the range of sizes considered.

(iii) Particle shape

Kahnert et al. (2007) show the errors of assuming that E-S particles can be comparable to the uncertainties in the refractive index of dust minerals, demonstrating that particle asphericity can be important when calculating the DRE. Applying the 5% change in dust loading for an ensemble of oblate spheroids with aspect ratio 2.2 (section 4), radiative transfer calculations show the corresponding change in surface DRE_{LW} to be 0.90 ± 0.01 W m^{-2}. Figure 11c shows the change in surface DRE_{LW}, relative to spheres (aspect ratio 1.0), for oblate spheroids when the aspect ratio increases to 2.2 and 3 for 1-μm-sized particles (black curves). As particle size increases, the shape parameter becomes more significant, as demonstrated in Fig. 11c for 2-μm-sized particles (gray curves). For the study period's average optical depth of $\sim$0.4, it is estimated that any errors associated with uncertainties in particle asphericity are ≤ 1 W m^{-2}, but could be as high as ~ 3 W m^{-2} or higher for particles with more extreme aspect ratios and sizes. Although dust particle shapes are usually more complicated in reality, with a complex range of particle shapes, sizes, and aspect ratios, this analysis illustrates the sensitivity of surface DRE_{LW} to dust particles defined by a simpler geometry.

6. Summary

The diurnal variability of airborne dust amount was examined using AERI spectral data with emphasis on three separate dust events during the NAMMA field study. A previously developed method for detecting/retrieving dust IR AOT was applied. Two examples of daytime/nighttime time series of AERI-retrieved AOT were shown with comparisons made using retrieved AOT data at 0.5 μm from a collocated/coincident MFRSR and MPL, and from *CALIPSO*, to demonstrate the method's reliability. The average IR AOT (10 μm) for the study period was about 0.37 while the average visible AOT (0.55 μm) was $\sim$0.52, which accounts for the larger retrieval errors in heavy dust loading scenarios. A diurnal cycle with generally higher nighttime dust loading was identified during dust case 1 (6–8 September), possibly due to diurnal changes in the boundary layer dynamics, which could affect the dust loading or increased dust loading itself. Time series of retrieved AOT was then used in a broadband radiative transfer model to quantify the time-dependent instantaneous surface DRE_{LW} for the three dust cases. The surface DRE_{LW} for the study varied between 2 and 10 W m^{-2} with daytime/nighttime means of 6.9 and 8.4 W m^{-2}, respectively, showing on average a slightly larger nighttime DRE_{LW} of $\sim$1.5 W m^{-2}. Surface DRE_{LW} was found to vary linearly with AOT, which when extrapolated to unit AOT, yielded a DRE_{LW} of ~ 16 W m^{-2} τ^{-1}, nearly 42% of the diurnally averaged SW values measured during the SHADE field campaign. LW heating rates for dust were evaluated for the three dust cases and were shown to vary on average from 0.25 to 0.30 K day^{-1} with maximum heating reaching nearly 0.6 K day^{-1}, enough to impact the local surface energetics. The TOA DRE_{LW} was also assessed for the three dust cases and was found to vary from 2 to 11 W m^{-2}. Like the surface DRE_{LW}, TOA DRE_{LW} varies linearly with AOT. The DRE_{LW} at the TOA is about 13 W m^{-2} τ^{-1}, which can be >36% of the diurnally averaged SW value obtained from previous studies.

Surface DRE_{LW} computational errors correspond to uncertainties in particle microphysics and mineralogy. For the cases considered, the sensitivity studies showed that uncertainties in mineral composition are likely to be the largest source for error when calculating surface DRE_{LW} and will strongly depend on which minerals are dominant and their exact mixture. For dust particles composed of pure minerals, the errors can be as high as 20 W m^{-2} in high dust loading scenarios (AOT $\geq$ 1). Uncertainties in particle size can impact the surface DRE_{LW} by $\pm$2 W m^{-2} for size distributions dominated by fine-mode particles or up to 5 W m^{-2} for those dominated by coarse-mode particles. Uncertainties in dust particle shapes can yield errors in the surface DRE_{LW} in the range of 1–3 W m^{-2} or higher depending on particle aspect ratio and size. For the shapes considered, a high dust loading scenario could impact the surface DRE_{LW} by a factor of 2 over that for E-S particles. Certainly nonnegligible, the surface DRE_{LW} can be an important parameter for assessing regional changes in surface temperatures and moisture budgets, and it has potential for modulating the atmospheric energetics. The DRE_{LW} therefore represents an important component in the study of regional climate variation.

Acknowledgments. We are grateful to Dr. Jose Pimenta Lima and his staff at INMG for their logistical support and for providing daily radiosonde data. Participation of SMART–COMMIT was supported by Dr. Hal Maring, NASA Radiation Science Program. The NASA Micro-Pulse Lidar Network, managed by Dr. E. J. Welton, was funded by NASA Earth Observing System and Radiation Sciences Program. Dr. Reid's participation was funded through the NASA *CALIPSO* science team and Naval Research Laboratory Base Program. We acknowledge the AERONET program managed by Dr. B. Holben. *CALIPSO* data were obtained from the NASA Langley Research Center Atmospheric Science Data Center. We are grateful to Dr. J. Haywood for his constructive and insightful comments. We also thank Drs. T. Roush and C. Zender for the mineral datasets, W. Feltz for providing the AERIPLUS code, and Dr. M. Mishchenko for his T-matrix light-scattering code. Lastly we thank the anonymous reviewers for their helpful remarks.

REFERENCES

Ackerman, S. A., and H. Chung, 1992: Radiative effects of airborne dust on regional energy budgets at the top of the atmosphere. *J. Appl. Meteor.,* **31,** 223–233.

Alexandrov, M. D., P. Kiedron, J. J. Michalsky, G. Hodges, C. J. Flynn, and A. A. Lacis, 2007: Optical depth measurements by shadow-band radiometers and their uncertainties. *Appl. Opt.,* **46,** 8027–8038.

Anderson, T. L., and Coauthors, 2005: An ''A-Train'' strategy for quantifying direct aerosol forcing of climate. *Bull. Amer. Meteor. Soc.,* **86,** 1795–1809.

Brindley, H. E., 2007: Estimating the top-of-atmosphere longwave radiative forcing due to Saharan dust from satellite observations over a West African surface site. *Atmos. Sci. Lett.,* **8,** 74–79.

Campbell, J. R., D. L. Hlavka, E. J. Welton, C. J. Flynn, D. D. Turner, J. D. Spinhirne, V. S. Scott, and I. H. Hwang, 2002: Full-time, eye-safe cloud and aerosol lidar observation at Atmospheric Radiation Measurement program sites: Instruments and data processing. *J. Atmos. Oceanic Technol.,* **19,** 431–442.

Chiapello, I., G. Bergametti, B. Chatenet, F. Dulac, I. Jankowiak, C. Liousse, and E. S. Soares, 1999: Contribution of the different aerosol species to the aerosol mass load and optical depth over the northeastern tropical Atlantic. *J. Geophys. Res.,* **104,** 4025–4035.

D'Almeida, G. A., P. Koepke, and E. P. Shettle, 1991: *Atmospheric Aerosols: Global Climatology and Radiative Characteristics*. A. Deepak, 561 pp.

Dufresne, J.-L., C. Gautier, P. Ricchiazzi, and Y. Fouquart, 2002: Longwave scattering effects of mineral aerosols. *J. Atmos. Sci.,* **59,** 1959–1966.

Feltz, W. F., W. L. Smith, H. B. Howell, R. O. Knuteson, H. Woolf, and H. E. Revercomb, 2003: Near-continuous profiling of temperature, moisture, and atmospheric stability using the atmospheric emitted radiance interferometer (AERI). *J. Appl. Meteor.,* **42,** 584–597.

Forster, P., and Coauthors, 2007: Changes in atmospheric constituents and in radiative forcing. *Climate Change 2007: The Physical Science Basis.* S. Solomon et al., Eds., Cambridge University Press, 129–234.

Fouquart, Y., B. Bonnel, G. Brogniez, J. C. Buriez, L. Smith, J. J. Morcrette, and A. Cerf, 1987: Observations of Saharan aerosols: Results of ECLATS field experiment. Part II: Broadband radiative characteristics of the aerosols and vertical radiative flux divergence. *J. Climate Appl. Meteor.,* **26,** 38–52.

Fu, Q., and K. N. Liou, 1992: On the correlated *k*-distribution method for radiative transfer in nonhomogeneous atmospheres. *J. Atmos. Sci.,* **49,** 2139–2156.

——, and ——, 1993: Parameterization of the radiative properties of cirrus clouds. *J. Atmos. Sci.,* **50,** 2008–2025.

Hansell, R. A., S.-C. Tsay, Q. Ji, K. N. Liou, and S.-C. Ou, 2003: Surface aerosol radiative forcing derived from collocated ground-based radiometric observations during PRIDE, SAFARI, and ACE-Asia. *Appl. Opt.,* **42,** 5533–5544.

——, K. N. Liou, S.-C. Ou, S.-C. Tsay, Q. Ji, and J. S. Reid, 2008: Remote sensing of mineral dust aerosol using AERI during the UAE^2: A modeling and sensitivity study. *J. Geophys. Res.,* **113,** D18202, doi:10.1029/2008JD010246.

Harrison, L., and J. Michalsky, 1994: Objective algorithms for the retrieval of optical depths from ground-based measurements. *J. Appl. Opt.,* **33,** 5126–5132.

Haywood, J. M., P. N. Francis, M. D. Glew, and J. P. Taylor, 2001: Optical properties and direct radiative effect of Saharan dust: A case study of two Saharan dust outbreaks using aircraft data. *J. Geophys. Res.,* **106** (D16), 18 417–18 430.

——, and Coauthors, 2003: Radiative properties and direct radiative effect of Saharan dust measured by the C-130 aircraft during SHADE: 1. Solar spectrum. *J. Geophys. Res.,* **108,** 8577, doi:10.1029/2002JD002687.

——, R. P. Allan, I. Culverwell, T. Slingo, S. Milton, J. Edwards, and N. Clerbaux, 2005: Can desert dust explain the outgoing longwave radiation anomaly over the Sahara during July 2003? *J. Geophys. Res.,* **110,** D05105, doi:10.1029/2004JD005232.

——, and Coauthors, 2008: Overview of the Dust and Biomass-Burning Experiment and African Monsoon Multidisciplinary Analysis special observing period-0. *J. Geophys. Res.,* **113,** D00C17, doi:10.1029/2008JD010077.

Heinold, B., I. Tegen, K. Schepanski, and O. Hellmuth, 2008: Dust radiative feedback on Saharan boundary layer dynamics and dust mobilization. *Geophys. Res. Lett.,* **35,** L20817, doi:10.1029/2008GL035319.

Highwood, E. J., J. M. Haywood, M. D. Silverstone, S. M. Newman, and J. P. Taylor, 2003: Radiative properties and direct effect of Saharan dust measured by the C-130 aircraft during Saharan Dust Experiment (SHADE): 2. Terrestrial spectrum. *J. Geophys. Res.,* **108,** 8578, doi:10.1029/2002JD002552.

Holben, B. N., and Coauthors, 1998: AERONET—A federated instrument network and data archive for aerosol characterization. *Remote Sens. Environ.,* **66,** 1–16.

Hsu, N. C., J. R. Herman, and C. Weaver, 2000: Determination of radiative forcing of Saharan dust using combined TOMS and ERBE data. *J. Geophys. Res.,* **105** (D16), 20 649–20 661.

Jeong, M.-J., Z. Li, E. Andrews, and S.-C. Tsay, 2007: Effect of aerosol humidification on the column aerosol optical thickness over the Atmospheric Radiation Measurement Southern Great Plains site. *J. Geophys. Res.,* **112,** D10202, doi:10.1029/2006JD007176.

——, S.-C. Tsay, Q. Ji, N. C. Hsu, R. A. Hansell, and J. Lee, 2008: Ground-based measurements of airborne Saharan dust in marine environment during the NAMMA field experiment. *Geophys. Res. Lett.,* **35,** L20805, doi:10.1029/2008GL035587.

Ji, Q., and S. C. Tsay, 2000: On the dome effect of Eppley pyrgeometers and pyranometers. *Geophys. Res. Lett.,* **27,** 971–974.

Jones, C., N. Mahowald, and C. Luo, 2003: The role of easterly waves on African desert dust transport. *J. Climate,* **16,** 3617–3628.

Kahnert, M., T. Nousiainen, and P. Räisänen, 2007: Mie simulations as an error source in mineral aerosol radiative forcing calculations. *Quart. J. Roy. Meteor. Soc.,* **133,** 299–307.

Knuteson, R. O., and Coauthors, 2004: Atmospheric Emitted Radiance Interferometer (AERI). Part II: Instrument performance. *J. Atmos. Oceanic Technol.,* **21,** 1777–1789.

Lau, K. M., M. K. Kim, and K. M. Kim, 2006: Asian summer monsoon anomalies induced by aerosol direct forcing: The role of the Tibetan Plateau. *Climate Dyn.,* **26,** 855–864.

Liu, X., J. Wang, and S. Christopher, 2003: Shortwave direct radiative forcing of Saharan dust aerosols over the Atlantic Ocean. *Int. J. Remote Sens.,* **24,** 5147–5160.

Mahowald, N. M., D. R. Muhs, S. Levis, P. J. Rasch, M. Yoshioka, C. S. Zender, and C. Luo, 2006: Change in atmospheric mineral aerosols in response to climate: Last glacial period, preindustrial, modern and doubled-carbon dioxide climates. *J. Geophys. Res.,* **111,** D10202, doi:10.1029/2005JD006653.

McClatchley, R. A., R. W. Fenn, J. E. A. Volz, and J. S. Garing, 1972: Optical properties of the atmosphere. Air Force Cambridge Research Laboratory Environmental Research Paper 411, 107 pp.

McFarlane, S. A., E. I. Kassianov, J. Barnard, C. Flynn, and T. P. Ackerman, 2009: Surface shortwave aerosol radiative forcing during the Atmospheric Radiation Measurement Mobile Facility deployment in Niamey, Niger. *J. Geophys. Res.,* **114,** D00E06, doi:10.1029/2008JD010491.

Mishchenko, M. I., and L. D. Travis, 1994: Light scattering by polydispersions of randomly oriented spheroids with sizes comparable to wavelengths of observation. *Appl. Opt.,* **33,** 7206–7225.

Mohalfi, S., H. S. Bedi, T. N. Krishnamurti, and S. Cocke, 1998: Impact of shortwave radiative effects of dust aerosols on the summer season heat low over Saudi Arabia. *Mon. Wea. Rev.,* **126,** 3153–3168.

Prospero, J. M., 1999: Long-range transport of mineral dust in the global atmosphere: Impact of African dust on the environment of the southeastern United States. *Proc. Natl. Acad. Sci. USA,* **96,** 3396–3403.

Redelsperger, J. L., C. D. Thorncroft, A. Diedhiou, T. Lebel, D. J. Parker, and J. Polcher, 2006: African Monsoon Multidisciplinary Analysis: An international research project and field campaign. *Bull. Amer. Meteor. Soc.,* **87,** 1739–1746.

Reid, E. A., J. S. Reid, M. M. Meier, M. R. Dunlap, S. S. Cliff, A. Broumas, K. Perry, and H. Maring, 2003: Characterization of African dust transported to Puerto Rico by individual particle and size segregated bulk analysis. *J. Geophys. Res.,* **108,** 8591, doi:10.1029/2002JD002935.

Reid, J. S., and Coauthors, 2003: Analysis of measurements of Saharan dust by airborne and ground-based remote sensing methods during the Puerto Rico Dust Experiment (PRIDE). *J. Geophys. Res.,* **108,** 8586, doi:10.1029/2002JD002493.

——, and Coauthors, 2006: Reconciliation of coarse-mode sea-salt aerosol particle size measurements and parameterizations at a subtropical ocean receptor site. *J. Geophys. Res.,* **111,** D02202, doi:10.1029/2005JD006200.

——, E. A. Reid, A. Walker, S. Piketh, S. Cliff, A. Al Mandoos, S.-C. Tsay, and T. F. Eck, 2008: Dynamics of southwest Asian dust particle size characteristics with implications for global dust research. *J. Geophys. Res.,* **113,** D14212, doi:10.1029/2007JD009752.

Rose, F. G., and T. P. Charlock, 2002: New Fu–Liou code tested with ARM Raman lidar and CERES in pre-CALIPSO sensitivity study. Preprints, *11th Conf. on Atmospheric Radiation,* Ogden, UT, Amer. Meteor. Soc., P4.8.

Shettle, E. P., and R. W. Fenn, 1979: Models for the aerosols of the lower atmosphere and the effects of the humidity variations on their optical properties. Air Force Geophysics Laboratory Environmental Research Paper No. 675, 94 pp.

Slingo, A., and Coauthors, 2006: Observations of the impact of a major Saharan dust storm on the atmospheric radiation balance. *Geophys. Res. Lett.,* **33,** L24817, doi:10.1029/2006GL027869.

Smirnov, A., B. N. Holben, T. F. Eck, O. Dubovik, and I. Slutsker, 2000: Cloud-screening and quality control algorithms for the AERONET database. *Remote Sens. Environ.,* **73,** 337–349.

Sokolik, I. N., and O. B. Toon, 1996a: Direct radiative forcing by anthropogenic airborne mineral aerosols. *Nature,* **381,** 681–683.

——, and ——, 1996b: Direct radiative forcing by airborne mineral aerosols. *J. Aerosol Sci.,* **27** (Suppl. 1), S11–S12.

——, and ——, 1997: Regional direct radiative forcing by the airborne mineral aerosols. *J. Aerosol Sci.,* **28** (Suppl. 1), S655–S656.

——, and ——, 1999: Incorporation of mineralogical composition into models of the radiative properties of mineral aerosols from UV to IR wavelengths. *J. Geophys. Res.,* **104,** 9423–9444.

Solomon, S., D. Qin, M. Manning, M. Marquis, K. Averyt, M. M. B. Tignor, H. L. Miller Jr., and Z. Chen, Eds., 2007: *Climate Change 2007: The Physical Sciences Basis*. Cambridge University Press, 996 pp.

Su, J., J. Huang, Q. Fu, P. Minnis, J. Ge, and J. Bi, 2008: Estimation of Asian dust aerosol effect on cloud radiation forcing using Fu–Liou radiative model and CERES measurements. *Atmos. Chem. Phys.,* **8,** 2763–2771.

Tanré, D., and Coauthors, 2003: Measurement and modeling of the Saharan dust radiative impact: Overview of the Saharan Dust Experiment (SHADE). *J. Geophys. Res.,* **108,** 8574, doi:10.1029/2002JD003273.

Turner, D. D., 2008: Ground-based infrared retrievals of optical depth, effective radius, and composition of airborne mineral dust above the Sahel. *J. Geophys. Res.,* **113,** D00E03, doi:10.1029/2008JD010054.

Vaughan, M., S. Young, D. Winker, K. Powell, A. Omar, Z. Liu, Y. Hu, and C. Hostetler, 2004: Fully automated analysis of space-based lidar data: An overview of the CALIPSO retrieval algorithms and data products. *Laser Radar Techniques for Atmospheric Sensing,* U. N. Singh, Ed., International Society for Optical Engineering (SPIE Proceedings, Vol. 5575), doi:10.1117/12.572024.

Vogelmann, A. M., P. J. Flatau, M. Szczodrak, K. M. Markowicz, and P. J. Minnett, 2003: Observations of large aerosol IR forcing at the surface. *Geophys. Res. Lett.,* **30,** 1655, doi:10.1029/2002GL016829.

Volz, F. E., 1973: Infrared optical constants of ammonium sulfate, Sahara dust, volcanic pumice, and fly ash. *Appl. Opt.,* **12,** 564–568.

Warren, S. G., 1984: Optical constants of ice from the ultraviolet to the microwave. *Appl. Opt.,* **23,** 1206–1225.

Welton, E. J., J. R. Campbell, J. D. Spinhirne, and V. S. Scott, 2001: Global monitoring of clouds and aerosols using a network of micro-pulse lidar systems. *Lidar Remote Sensing for Industry and Environmental Monitoring,* U. N. Singh, T. Itabe, and N. Sugimoto, Eds., International Society for Optical Engineering (SPIE Proceedings, Vol. 4153), 151–158.

Winker, D. M., W. H. Hunt, and M. J. McGill, 2007: Initial performance assessment of CALIOP. *Geophys. Res. Lett.,* **34,** L19803, doi:10.1029/2007GL030135.

World Climate Program, 1986: A preliminary cloudless standard atmosphere for radiation computation. WCP-112, WMO/TD-24, 60 pp.

Yu, H., and Coauthors, 2006: A review of measurement-based assessment of aerosol direct radiative effect and forcing. *Atmos. Chem. Phys.,* **6,** 613–666.

Zhang, J., and S. A. Christopher, 2003: Longwave radiative forcing of Saharan dust aerosols estimated from MODIS, MISR, and CERES observations on *Terra*. *Geophys. Res. Lett.,* **30,** 2188, doi:10.1029/2003GL018479.